Modeling, analysis, and validation of an active T-shaped noise barrier

Rongping Fan, Zhongqing Su,[a] and Li Cheng
The Department of Mechanical Engineering, The Hong Kong Polytechnic University, Hung Hom, Kowloon, Hong Kong Special Administration Region

(Received 14 March 2013; revised 6 June 2013; accepted 22 July 2013)

With ever-increasing land traffic, abatement of traffic noise using noise barriers remains significant, yet it is a challenging task due to spatial competition with other infrastructure. In this study, a deep insight into the diffraction characteristics of acoustic fields near noise barriers of various geometries and surface conditions was achieved using numerical simulations. A T-shaped passive noise barrier with acoustically soft upper surfaces was demonstrated to outperform other candidates in a middle- or high-frequency range. Based on attributes of the acoustic field diffracted by T-shaped barriers, an active control strategy was developed to revamp the T-shaped barrier, in which a filtered mini-max algorithm was established to drive the secondary sound sources. This algorithm resulted in more uniformly distributed residual sound fields than a filtered-X least mean square algorithm. Performance of the actively controlled barrier was evaluated at different positions and spacings of secondary sound sources and error sensors, leading to a series of optimal criteria for the design of active noise barriers. A prototype was fabricated and validated experimentally, manifesting particular effectiveness in insulating low-frequency noise, supplementing well the capacity of a passive T-shaped barrier which is effective in the middle- or high-frequency range.
 [http://dx.doi.org/10.1121/1.4817887]

PACS number(s): 43.50.Gf [NX] Pages: 1990–2003

I. INTRODUCTION

To protect sensitive land users from traffic noise pollution, various noise barriers based on different design philosophies have been erected along highways to mitigate or block transport noise, playing an important role in maintaining the quality of residential life in urban areas.[1–9] The main tendencies among recent efforts in developing noise barriers are to innovatively revamp the geometry of the barrier edge and to adopt efficient absorbing materials. Shizuka and Fujiwara[3] compared the performance of noise barriers with various edge shapes and acoustic surface conditions using a boundary element method (BEM). They concluded that using either acoustically soft edges or absorbing materials could enhance the noise abatement. A barrier of T-shaped design outperformed others including straight, branch-shaped, and multiple-edge barriers. More specifically, a T-shaped barrier 3 m in height with soft edges could provide the same capacity as a 10 m high straight barrier without any special treatment on its edges and surfaces.

It can be tedious in practice to achieve an acoustically soft edge in a wide frequency range. Fujiwara *et al.*[4] investigated a series of T-shaped barriers with uniform rigid wells on their upper surfaces, and proposed an appropriate design of the wells so as to facilitate formation of acoustically soft edges, though it was effective in a narrow frequency band only. Monazzam and Lam[5] examined the insertion loss of the sound field around noise barriers with quadratic residue diffuser (QRD) tops in cylindrical, T-, arrow-, and Y-shaped profiles, respectively. In comparison with a rigid or an absorbing surface condition, the QRD tops increased the insertion loss behind the barrier more effectively; supplemented with a T-shaped or arrow-shaped design, the barrier with QRD tops further increased the insertion loss. Okubo and Yamamoto[6] and Okuba *et al.*[7] studied the efficiency of various barriers with different edge shapes and acoustical devices mounted on their top edges, and revealed that the acoustic efficiency of the edge device depends substantially on the angles of the sources and receivers. Based on that finding, a new approach for determining the efficiency of edge devices attached to a noise barrier was established.

Hitherto most efforts toward achieving optimal design of noise barriers have used passive means, taking advantage of different shapes of the barrier edge and various absorbing materials. These barriers can provide significant noise abatement in the middle- or high-frequency range. Relying on a passive design philosophy, a barrier must often be sufficiently high to block noise propagation, but that requirement can be impractical and uneconomical in some instances, with increasing competition for space with other infrastructure. Thus, in order to achieve a more insertion loss over a wider frequency range, including relatively low frequency ranges, active control has been introduced into barrier design. Ise *et al.*[10] developed a single-channel adaptive control system comprising a loudspeaker serving as a monopole control source and a microphone as an error sensor. A quiet area around the microphone was achieved in the frequency band below 500 Hz. Han and Qiu[11] used the absolute mean value of the sound intensity as the cost function in the control algorithm, to achieve greater insertion loss than when sound pressure was adopted as the cost function.

[a]Author to whom correspondence should be addressed. Electronic mail: mmsu@polyu.edu.hk

Omoto *et al.*[12] employed multiple secondary sources to actively suppress sound at the diffraction edge of a semi-infinite noise barrier (rather than mitigating the diffracted noise in the dark area), revealing that the closer the secondary source was to the primary sound source, the more attenuation of the sound could be expected as a result of active control. In a numerical study, Shao *et al.*[13] demonstrated that achieving a minimum of the sum of all squared acoustic pressures at all error sensors was more effective in canceling noise than a minimum of the sound pressure itself at individual error sensors; and with the same number of secondary sources, an arc-type arrangement of error sensors was advantageous compared with a straight line configuration. Duhamel[14] and Tao *et al.*,[15] respectively, examined different locations of secondary sources, and established criteria for optimal arrangement of these secondary sources based on different objective functions. Considering the optimal spacing between two adjacent secondary sources and between two error sensors, Guo *et al.*[16–18] and Niu *et al.*,[19] respectively, calibrated the capacities of noise barriers with different locations of secondary source and error sensors, and suggested criteria for determining these spacings.

The majority of the above active control strategies, based on different mechanisms and manifesting different efficiency, have adopted a multichannel *filtered-X least mean square* (FXLMS) algorithm (also known as *multiple error LMS*)[20,21] in which the cost functions were set as the sum of the mean squares of the error signals measured by individual error sensors. This control philosophy has been proven robust even when certain discrepancies exist between the modeling and reality. In practical implementation, however, the difference between the maximum and minimum sound pressure levels captured by a series of error sensors can sometimes be large, potentially leading to non-uniformly distributed residual sound fields upon application of FXLMS-based active control. This shortcoming can prevent an active noise barrier from delivering the desired control effect.

In this study, a combined consideration of (a) the commendable effectiveness of a T-shaped noise barrier in abating middle- or high-frequency noise, (b) the advantage of active control in isolating low-frequency noise, and (c) the deficiency of an FXLMS algorithm motivates the design, analysis, and development of a noise barrier with appropriate geometric features driven by a practically robust active control algorithm. A comprehensive investigation of the diffraction characteristics of acoustic fields near barriers with various geometries and surface conditions is carried out using numerical simulation. On the basis of the simulation results, a T-shaped noise barrier with acoustically soft upper surfaces is designed. An active control strategy and a system using a filtered minimax algorithm[22–24] are established to actively drive the secondary sound sources in response to different primary sound sources. Different configurations of the secondary sources and error sensors are compared for efficiency, leading to a series of optimal criteria for positions and intervals of the secondary sources and error sensors in the active control system. A prototype of an actively controlled barrier is fabricated and validated experimentally.

II. SIMULATION FOR OPTIMAL DESIGN OF NOISE BARRIER

The sound diffraction characteristics near a traditional straight barrier and a T-shaped barrier with different surface conditions are examined using a BEM.

A. Modeling and simulation

A two-dimensional straight barrier and a T-shaped barrier, both 2 m high and 0.1 m thick, are considered, as shown schematically in Figs. 1(a) and 1(b), respectively. The width of the top edge of the T-shaped barrier is 0.5 m. The coordinate system originates from the lower left corner of each barrier. The noise source is assumed to be a coherent line source with a sound pressure of 1 Pa, 0.5 m above the ground, and 2 m from the left surface of each barrier. An area measuring 4.2×4.5 m^2 behind each barrier is defined as the observation area, as indicated in Fig. 1.

Four scenarios of the top surface conditions of the T-shaped barrier are hypothesized:

(1) Scenario 1: An ideal rigid surface (i.e., Neumann boundary condition), on which the normal particle velocity is zero;
(2) Scenario 2: An acoustically soft surface, on which the surface pressure is zero;
(3) Scenario 3: An ideal acoustically absorbing surface, on which the surface pressure is the same as the incident pressure; and
(4) contrasting the above three ideal cases, Scenario 4: A non-ideal absorbing surface with fibrous absorbing material (actual cases in practice).

For the three ideal scenarios, a surface impedance parameter, Z, is introduced, defined as[25]

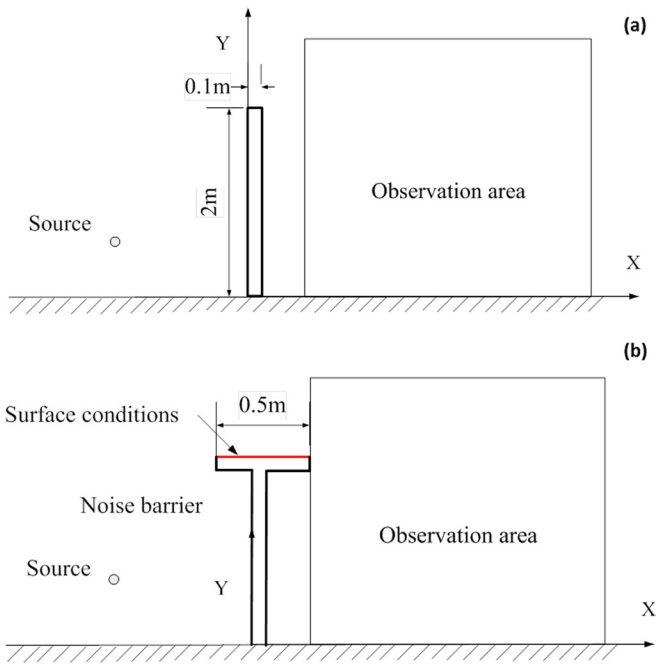

FIG. 1. (Color online) Schematic diagram of T-shape noise barrier in two dimensions: (a) Straight barrier, and (b) T-shape noise barrier with various surface conditions.

$$Z = \frac{p}{v_n}, \tag{1}$$

where p and v_n are the acoustic pressure at the surface and the acoustic velocity component normal to the top surface, respectively. v_n is positive if the velocity points to the top surface. Z is infinitely large for Scenario 1, zero for Scenario 2, and unity (i.e., 1.0) for Scenario 3. Alternatively, Z can be expressed in a complex form as $Z = R' + iX'$ (where R' is the resistive part, and X' the reactive part of the impedance), to comprehend the damping effect of the barrier and to account for the phase shift of sound waves due to the acoustically treated surfaces. Using the complex form, for Scenario 4, the non-ideal case in which sound waves are reflected from the absorbing surface, the surface impedance parameter is defined using an empirical model,[26] as

$$Z = \rho_0 c\left[1 + 0.0571\left(\frac{\rho_0 f}{\sigma}\right)^{-0.754} + \mathrm{i}0.0870\left(\frac{\rho_0 f}{\sigma}\right)^{-0.732}\right], \tag{2}$$

where ρ_0 is the density of air, c is the speed of sound, f is the frequency of sound, and σ is the specific flow resistivity per unit thickness of the material. In Eq. (2), Z is normalized with respect to the characteristic impedance of air $\rho_0 c$, and it is subject to the frequency of the sound source, as seen in Figs. 2(a) and 2(b), respectively, for the resistance and reactance terms of Z ($\sigma = 200\,\mathrm{kN\cdot s/m^4}$, corresponding to a grass-covered surface condition). It can be seen that both the resistance and the reactance terms of Z decrease with an increase in frequency.

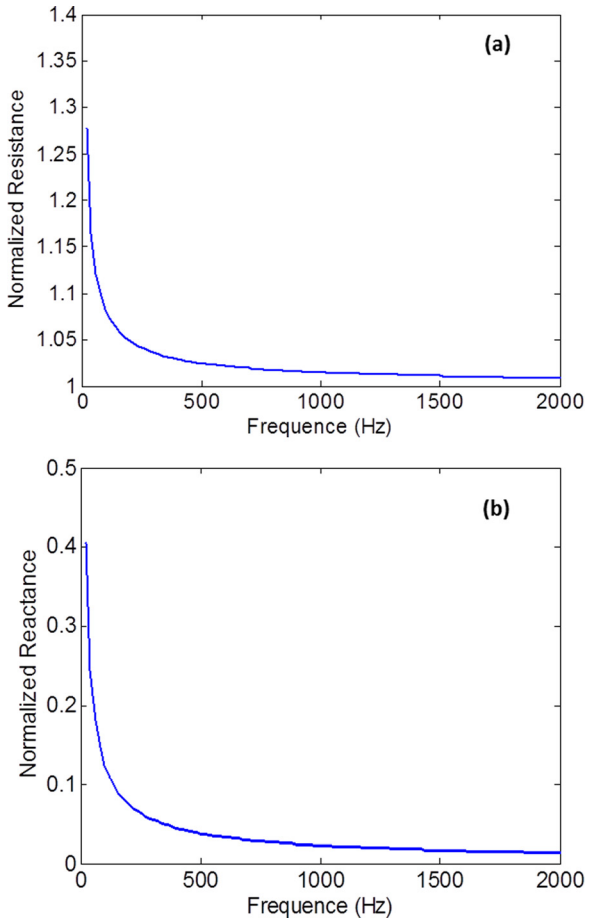

FIG. 2. (Color online) Normalized surface impedance of absorbing surface with flow resistivity $\sigma = 200\,\mathrm{kN\ s/m^4}$: (a) R, normalized resistance and (b) X, normalized reactance.

The straight and T-shaped barriers with four surface conditions are modeled using commercial BEM software SYSNOISE®. Line elements are adopted (a total of 410 elements for the straight barrier, 490 elements for the T-shaped barrier). The x axis overlaps the ground surface, which has a reflective character. A pure tone in a frequency range from 100 to 2000 Hz is generated by a coherent line source. The sound field in the observation area is evaluated in terms of insertion loss, defined as[4]

$$\Delta \mathrm{L} = 20\log(|p_g|/|p_b|), \tag{3}$$

where p_g and p_b are the total sound pressure captured by the same receiver in the observation area in the absence and presence of a barrier, respectively.

B. Straight vs T-shaped barriers

The calculated insertion loss in the observation area for the straight and T-shaped barriers with different surface scenarios, with a line source of 1000 Hz as an example, is presented in Fig. 3. It can be seen that (1) the straight barrier provides the poorest noise mitigation compared with the T-shaped barrier with any of the four surface scenarios; (2) among different surface conditions, the T-shaped barrier with the zero pressure top surface (Scenario 2) outperforms the rest, as shown in Fig. 3(e) in which the insertion loss exceeds 20 dB at the height of 1.0 m in the observation area. A comparison of the insertion loss in Figs. 3(b)–3(e) accentuates that the acoustic condition at the top of the T-shape noise barrier plays a vital role in influencing the diffracted sound field in the observation area. For other candidate frequencies in the discussed range (100 to 2000 Hz), similar phenomena are captured.

C. Characteristics of acoustic field near T-shaped barrier

The diffraction characteristics of the acoustic field of the T-shaped barrier with an acoustically soft surface (Scenario 2) which presents the highest insertion loss are further canvassed. Using the above modeling and simulation approach, Figs. 4(a)–4(c) display the sound pressure contour diagrams for Scenario 2 at three representative frequencies in the low, middle, and high-frequency ranges (125, 500, and 700 Hz). For comparison, the contour diagrams for the barrier with a rigid surface (Scenario 1) at the same frequencies are shown in Figs. 4(d)–4(f). It can be observed that the sound pressure levels within the observation area in Scenario 2 are consistently lower than those at the same locations in Scenario 1, at all the frequencies under investigation.

To facilitate further understanding, the equi-phase surfaces (i.e., the sound wavefront) of the sound fields for two

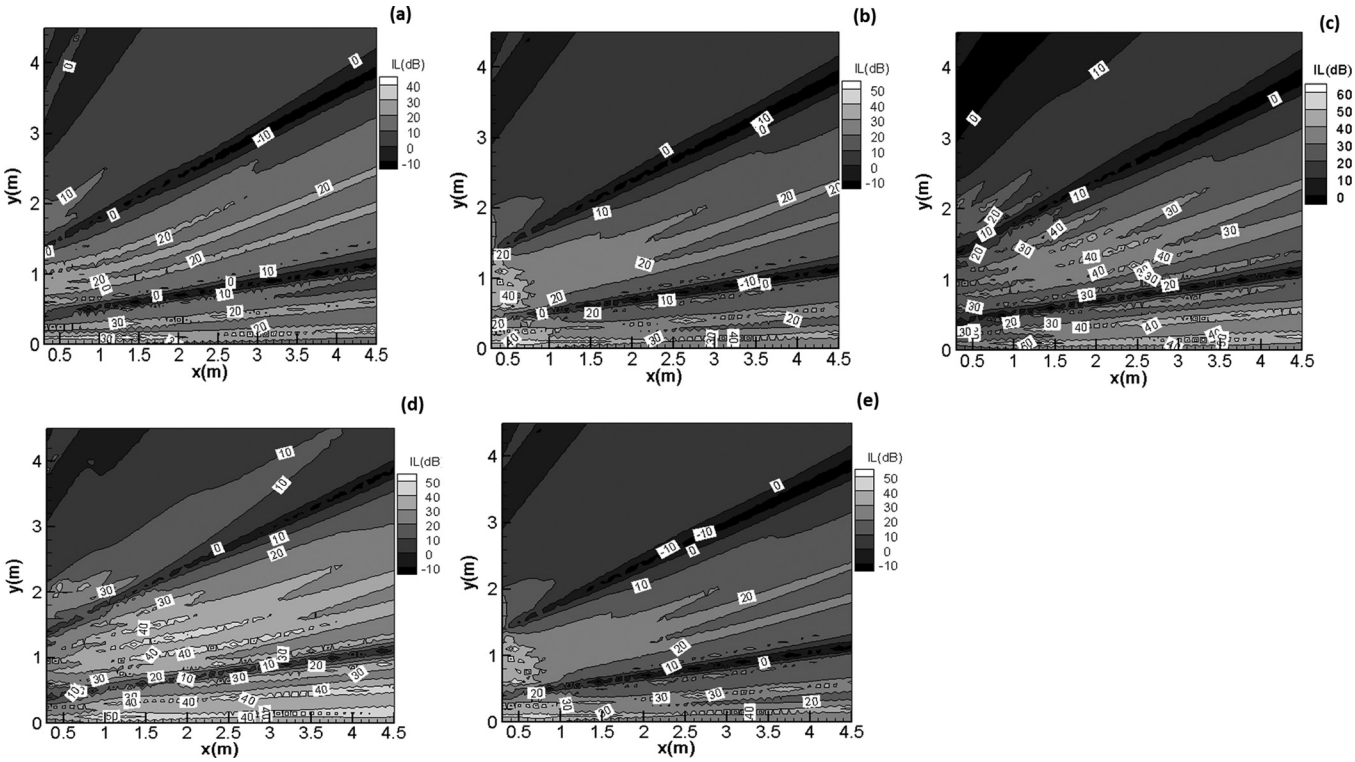

FIG. 3. The insertion loss of straight and T-shape noise barriers at 125 Hz: (a) Straight noise barrier, (b) rigid surface, (c) absorbing surface impedance = 1, (d) absorbing surface defined by flow resistivity $\sigma = 200$ kN s/m^4, and (e) zero pressure.

scenarios are calculated, displayed in Fig. 5, respectively. The following phenomena are observed:

(1) The wavefronts diffracted by the top of the T-shaped barrier form a series of concentric circles in the shadowed area (the region containing no direct wave propagation from the primary sound source), as highlighted in the figures; the higher the frequency of the sound source the denser the distribution of the concentric circles;
(2) both tips of the T-shaped barrier cap behave like imaginary edge sources to diffract the sound from the primary source, diffracting sound wavefronts radially from each tip; and
(3) the contour lines of the sound pressure level for two scenarios (in Fig. 4) do not have the same distribution patterns as that of their corresponding equi-phase surfaces (in Fig. 5), indicating that the imaginary edge source (two cap tips) diffracts sound waves with strong directivity rather than in a circular pattern in the shadowed area.

For further comparison, the differences in sound pressure between Scenarios 1 and 2 are shown in Figs. 6(a) and 6(b) for two representative frequencies (125 and 500 Hz), respectively. It is noticeable that the maximum difference in sound pressure level between the two surface conditions occurs at the top of the T-shaped barrier throughout the entire sound field.

As demonstrated,[27] the diffracted sound field in the observation area can be deemed to be that diffracted by a straight noise barrier, its thickness being the width of the top cap of the T-shaped barrier, provided the width of the top cap of the T-shaped noise barrier is greater than the wavelength, as illuminated in Fig. 7. With that conclusion, the sound field diffracted by the right imaginary source (S_A in Fig. 7) exists only in the observation area (beneath Line I in Fig. 7) for a T-shaped barrier, presenting a series of concentric circles as observed in Fig. 5. To canvass the diffracted sound field near the right imaginary source, the simulation is carried out in the vicinity of the right tip of the barrier cap, and the sound pressure differences between two scenarios are exhibited in Figs. 6(c) and 6(d) for the above two selected frequencies of 125 and 500 Hz, revealing that the maximum difference near the right imaginary source and accentuating the sound pressure around the right corner of the T-shaped barrier has a critical influence on the diffracted sound field in the observation area. These observations of the diffraction characteristics of the sound field in the vicinity of the T-shaped barrier provide essential criteria for developing an active control algorithm for a T-shaped noise barrier.

III. ACTIVE T-SHAPED NOISE BARRIER

Although the T-shaped noise barriers with the acoustically soft surface and the ideal acoustically absorbing surface (Scenarios 2 and 3) can efficiently reduce the diffracted sound, it is impossible for any practical materials to achieve ideal conditions (Scenarios 2 and 3 represent ideal conditions) over the entire frequency range, in particular in a low frequency range. As an alternative, the active control technique can be used to improve the efficiency of the noise barrier at low frequencies by cancellation of the sound pressure in the shadowed area or at a diffraction edge. Based on the previous analysis that the sound pressure above the top surface of the T-shaped noise barrier has an effect on the

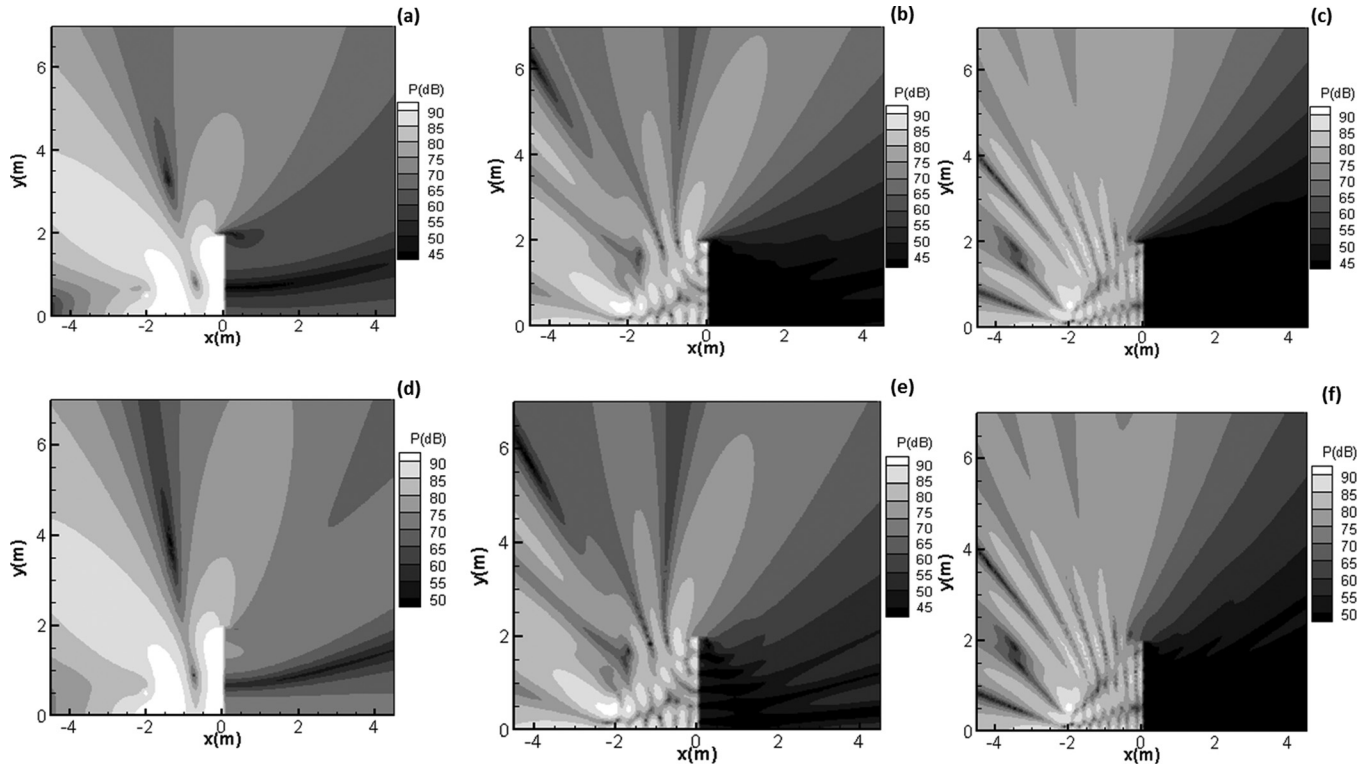

FIG. 4. Sound pressure contour of T-shape noise barrier: (a) 125 Hz for zero pressure surface, (b) 500 Hz for zero pressure surface, (c) 700 Hz for zero pressure surface, (d) 125 Hz for rigid top surface, (e) 500 Hz for rigid top surface, and (f) 700 Hz for rigid top surface.

diffracted sound field in the shadowed region (as observed in Fig. 6), extra insertion loss in the low-frequency domain can be obtained in the shadow region behind the T-shaped noise barrier by suppressing the sound pressure above the top surface of the barrier or the sound pressure at S_A. Therefore, active noise control is applied to achieve local sound pressure zero in the low frequency range.

A. Theory for simulation

Assume that there are the same number N of secondary sources and error microphones. N secondary sources and N error microphones are located in two parallel lines in the configuration of the multichannel active noise control system of the T-shaped barrier. The interval between two adjoining

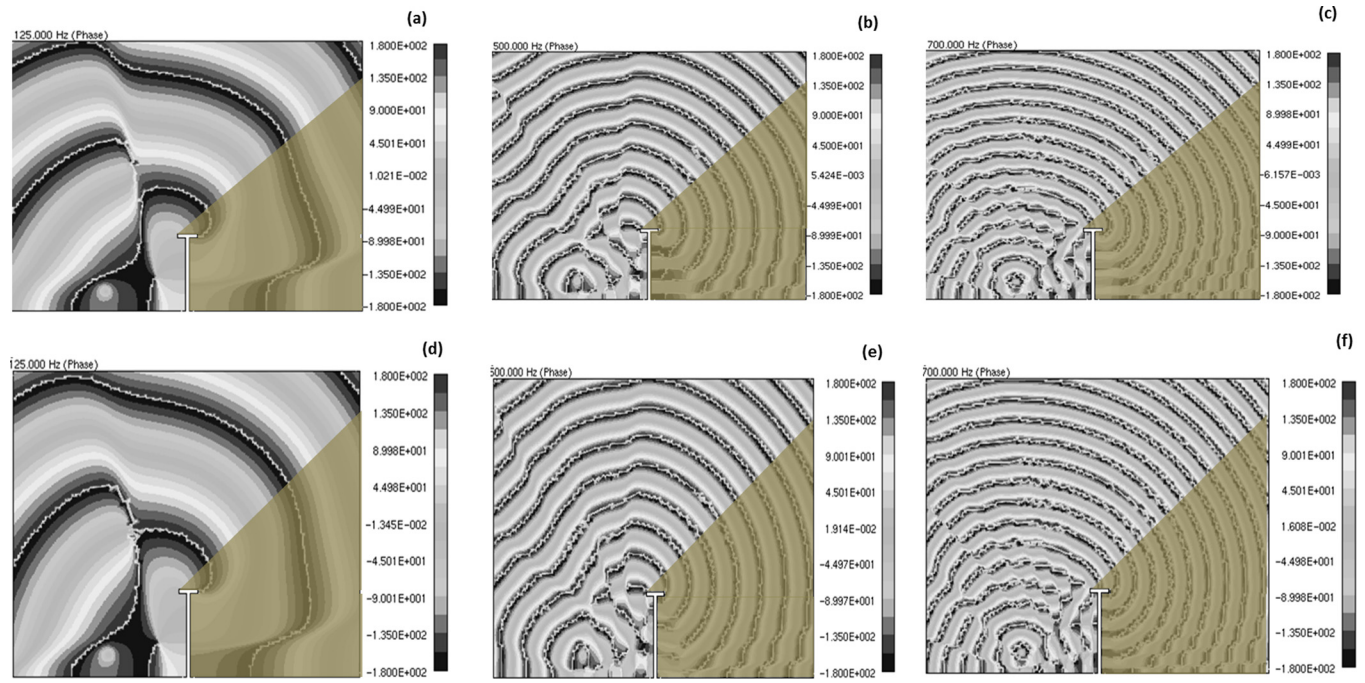

FIG. 5. (Color online) Equiphase surface of sound pressure contour of T-shape noise barrier: (a) 125 Hz for zero pressure surface, (b) 500 Hz for zero pressure surface, (c) 700 Hz for zero pressure surface, (d) 125 Hz for rigid top surface, (e) 500 Hz for rigid top surface, and (f) 700 Hz for rigid top surface.

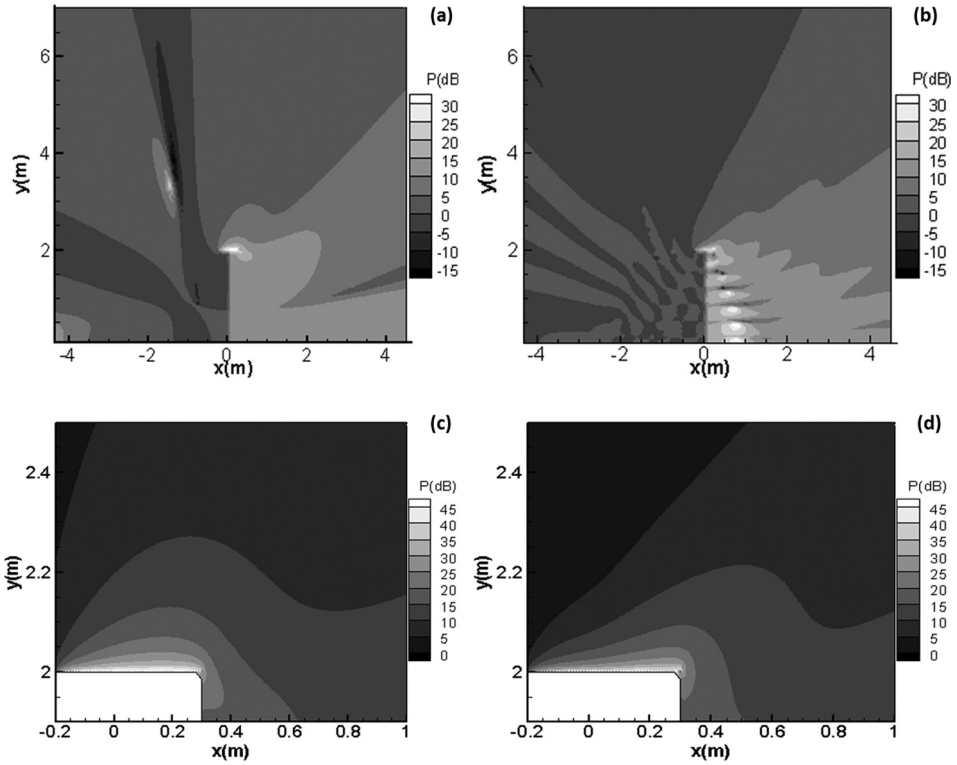

FIG. 6. Difference in sound pressure level around T-shape noise barrier between rigid and zero sound pressure of top surfaces: (a) 125 Hz, (b) 500 Hz, (c) 125 Hz in small region, and (d) 500 Hz in small region.

secondary sources is equal to that between two error sensors. The total sound pressure $p_t(\mathbf{r})$ at location $\mathbf{r}$ (any point in the observation region) is the superposition of the sound pressures $p_p(\mathbf{r})$ and $p_s(\mathbf{r})$ at location $\mathbf{r}$ from the primary and secondary sound fields

$$p_t(\mathbf{r}) = p_p(\mathbf{r}) + p_s(\mathbf{r}). \tag{4}$$

In the above, the sound pressure p_s ($\mathbf{r}$) at location $\mathbf{r}$ by N secondary sources is expressed as

$$\begin{aligned} p_s(\mathbf{r}) &= \sum_{i=1}^{N} q^i Z_s(\mathbf{r}, \mathbf{r}_c^i) \\ &= [Z_s(\mathbf{r}, \mathbf{r}_c^1), Z_s(\mathbf{r}, \mathbf{r}_c^2), ..., Z_s(\mathbf{r}, \mathbf{r}_c^i), ..., Z_s(\mathbf{r}, \mathbf{r}_c^N)\mathbf{q}, \end{aligned} \tag{5}$$

where q^i and $\mathbf{r}_c^i$ are the strength and location respectively of the ith secondary source, and $\mathbf{Z}_s$ is the transfer function between the receiving location and the secondary sources. The total sound pressures measured at the N error microphone positions are given by the vector $\mathbf{P}$

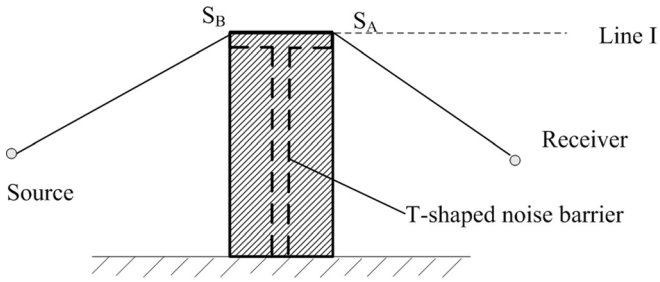

FIG. 7. Schematic diagram for wavefronts at middle and high frequency around the T-shape noise barrier.

$$\mathbf{p} = [p_t(\mathbf{r}_e^1), ..., p_t(\mathbf{r}_e^j), ..., p_t(\mathbf{r}_e^N)]^T, \tag{6}$$

where $\mathbf{r}_e^j$ is the location of jth error microphone. Substituting Eqs. (4) and (5) into Eq. (6), the vector $\mathbf{P}$ is expressed as

$$\mathbf{p} = \mathbf{p}_p + Z\mathbf{q}, \tag{7}$$

where $\mathbf{p}_p = [p_p(\mathbf{r}_e^1), ..., p_p(\mathbf{r}_e^j), ..., p_p(\mathbf{r}_e^N)]^T$ is the sound pressure vector of the primary sound field at the N error microphones, and $\mathbf{Z}$ is the acoustical transfer function matrix between the N secondary sources and the N error microphones

$$\mathbf{Z} = \begin{bmatrix} Z_s(\mathbf{r}_e^1, \mathbf{r}_c^1) \cdots Z_s(\mathbf{r}_e^1, \mathbf{r}_c^i) \cdots Z_s(\mathbf{r}_e^1, \mathbf{r}_c^N) \\ \vdots \\ Z_s(\mathbf{r}_e^j, \mathbf{r}_c^1) \cdots Z_s(\mathbf{r}_e^j, \mathbf{r}_c^i) \cdots Z_s(\mathbf{r}_e^j, \mathbf{r}_c^N) \\ \vdots \\ Z_s(\mathbf{r}_e^N, \mathbf{r}_c^1) \cdots Z_s(\mathbf{r}_e^N, \mathbf{r}_c^i) \cdots Z_s(\mathbf{r}_e^N, \mathbf{r}_c^N) \end{bmatrix}. \tag{8}$$

The objective of the active noise barrier is to minimize the sum of the squared acoustic pressures at the error sensors. The cost function of the control system is written as a Hermitian quadratic form of the control variable $\mathbf{q}$ of the secondary sound sources

$$J = \sum_{j=1}^{M} |p_t(\mathbf{r}_e^j)|^2 = \mathbf{p}^H \mathbf{p} = J_0 + \mathbf{b}^H \mathbf{q} + \mathbf{q}^H \mathbf{b} + \mathbf{q}^H \mathbf{A} \mathbf{q}, \tag{9}$$

where

$$J_0 = \mathbf{p}_p^H \mathbf{p}_p, \tag{10}$$

$$\mathbf{b} = \mathbf{Z}^H \mathbf{p}_p, \tag{11}$$

$$\mathbf{A} = \mathbf{Z}^H\mathbf{Z}. \tag{12}$$

In the above, superscript "H" denotes the Hermitian transpose. The matrix $\mathbf{A}$ is positive definite. This guarantees that J has a global minimum. The optimal secondary source strength for the cost function is given by

$$\mathbf{q}_{\min} = -\mathbf{A}^{-1}\mathbf{b}. \tag{13}$$

The minimized cost function is

$$J_{\min} = J_0 - \mathbf{b}^H\mathbf{A}^{-1}\mathbf{b}. \tag{14}$$

Given the optimal secondary source strength, one can then calculate the total sound pressure at any point $\mathbf{r}$ upon control applied. The acoustic performance of the active noise control on the T-shaped barrier is generally assessed by the extra insertion loss

$$\Delta L = 20\log(|p_{\text{off}}|/|p_{\text{on}}|), \tag{15}$$

where p_{off} is the total pressure field without active noise control, and p_{on} is the total pressure field with active noise control. The transfer function and the sound pressure in the observation area are evaluated in SYSNOISE®.

In the previous section (Sec. II), two-dimensional models of straight and T-shaped noise barriers of infinite length were used to investigate the diffracted sound field of passive noise barriers. Tremendous computational cost is required to build a three-dimensional ideal T-shaped noise barrier in SYSNOISE® which is so long that there are no diffracted sound fields around the vertical edge from the primary and secondary sound sources. To save the computational cost of SYSNOISE®, a three-dimensional model of a T-shaped barrier 4 m in height, 20 m in length, and 0.1 m in thickness, as shown in Fig. 8(a), is used as the noise barrier. The width of the top edge of the T-shaped noise barrier is 1 m. The meshed model of the T-shaped noise barrier built in SYSNOISE® is illustrated in Fig. 8(b).

Although many factors influence the noise reduction in active noise control, attention is paid here to the intervals and positions of error sensors and secondary sources. For convenience of describing the different configurations of the active T-shaped noise barriers, two positions of the error sensors and three positions of the secondary sources are described in this section.

On the basis of the characteristics of the diffracted sound field, the imaginary sound sources of the T-shaped barrier are located at each edge of the top cap. The sound field at the edge on the side of the primary sound source influences the sound field above the top of the noise barrier. Reduction of the sound pressure on either edge of the top cap can suppress the diffracted sound. As shown in Figs. 9(a) and 9(b), two locations A and B ($x = -0.5$ m, $y = 4$ m) and ($x = 0.5$ m, $y = 4$ m) of the error microphones on either edge of the top cap of the T-shaped noise barrier are investigated.

As demonstrated in Figs. 9(d)–9(f), three arrangements of the secondary sources are considered in the numerical simulation. As shown in Fig. 9(d), the location of the

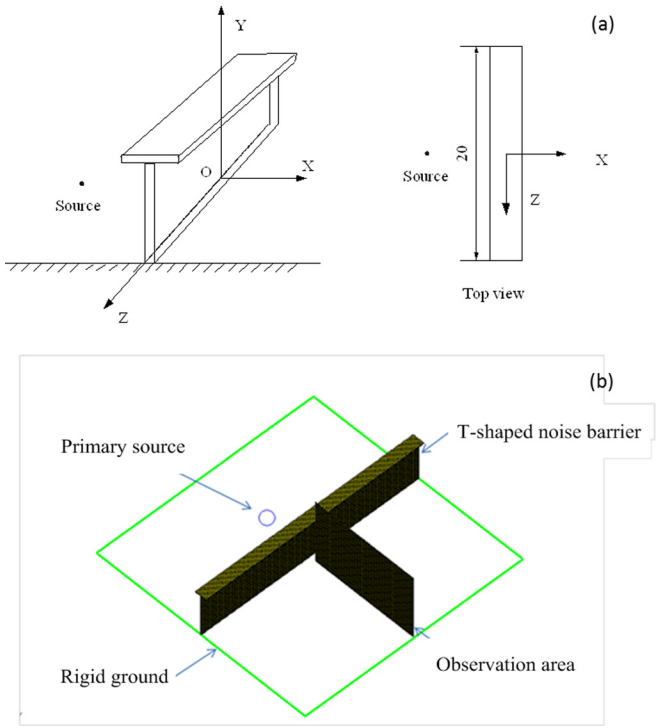

FIG. 8. (Color online) The configuration of T-shape noise barrier in three dimensions: (a) Schematic diagram and (b) BEM model in SYSNOISE®.

secondary sources is in the line ($x = -1$ m, $y = 3.46$ m) and lies in the line which passes through the primary sound source and the edge of the top cap on the same side as the source. Due to the external profile of the T-shaped noise barrier, the equip-phase contour near the tip of the top cap on the side of the primary sound source, as shown in Figs. 5(a) and 5(d), resembles concentric circles at low frequencies. This indicates that there is the larger wavefront matching area between the primary sound source and a secondary source when secondary sources are located at the center of the concentric circles. Therefore, the performance of the active control system with secondary sources at the two locations, as shown in Figs. 9(e) and 9(f), is investigated. The position SB is near the center of the concentric circles ($x = -0.76$ m, $y = 4$ m) and the position SC is on the edge of the T-shaped barrier on the source side.

B. Influence of locations and intervals of error sensors

The schematic diagram of one configuration of an active noise system is given in Fig. 10. Five secondary sources and five error sensors are used in the active noise barrier. The observation area on the side of the receiver is perpendicular to the T-shaped noise barrier and lies in the vertical plane where the primary sound source is located. The primary sound source is located at (−0.54 m, 2.0 m, 0). In the typical case where the secondary sources and error sensors are equally spaced in two parallel lines,[16] there is an optimal range of spacing for the secondary sources and error sensors. The minimal spacing $r_{\text{ss-min}}$ and maximal spacing $r_{\text{ss-max}}$ are given by

$$r_{\mathrm{ss-max}} \cong \begin{cases} \dfrac{\lambda}{2}\sqrt{1+\dfrac{4r_{\mathrm{se}}}{N\lambda}}, & N=2,4,6,\ldots., \\ \dfrac{\lambda}{2}\sqrt{1+\dfrac{N+1}{N-1}\dfrac{4r_{se}}{N\lambda}}, & N=3,5,7,\ldots., \end{cases} \tag{16}$$

$$r_{\mathrm{ss-min}} \cong \begin{cases} \dfrac{5\lambda}{2}\exp\left\{-\left[\dfrac{3(\lambda+0.04r_{\mathrm{ps}})}{2r_{\mathrm{se}}-\lambda}+\dfrac{20\lambda}{15\lambda+r_{\mathrm{ps}}}\right]\right\} & N=4,6,8,\ldots., \\ \dfrac{3\lambda(N+1)}{N}\exp\left\{-\left[\dfrac{\lambda+2r_{\mathrm{ps}})}{2(2r_{\mathrm{se}}-\lambda)}+\dfrac{12\lambda}{5\lambda+r_{\mathrm{ps}}}\right]\right\} & N=3,5,7,\ldots., \end{cases} \tag{17}$$

where λ is the wavelength, r_{se} is the interval between secondary sources and error sensors, r_{ps} is the distance from the primary sound source and the secondary source line, and N is the number of secondary sources and error sensors. The optimal range of spacing is applicable to this configuration of the active noise barrier with the error sensor located on the edge on the source side. The upper limit of the optimal range for the configuration investigated in this paper is 1.45 m.

This optimal range of spacing is based on the curve fitting of numerical results for various configurations without a noise barrier.[17,18] Because of the complex diffraction phenomena around the T-shaped barrier, it is uncertain whether the same optimal range of spacing is suitable for a configuration where the error sensors are located on the edge of the T-shaped barrier on the receiving side. Therefore the interval between secondary sources and error sensors is varied from 0.3 to 1.4 m to further investigate the performance of the active noise control. Numerical simulations of a pure tone at the frequency of 125 Hz are carried out. The results of numerical simulation for an active T-shaped barrier with error sensors located at positions A and B are presented in Figs. 11 and 12, respectively. Positive values of the contour diagram for the extra insertion loss in Figs. 11 and 12 represent the magnitude of reduction of diffracted sound. Negative values indicate that the active noise control increases the diffracted sound behind the T-shaped noise barrier.

It can be seen in Figs. 11 and 12 that for the same interval, configurations with the error sensors located at position B create larger quiet zone areas than those with the error sensors located at position A. This indicates that reduction of the sound pressure on the edge on the receiving side suppresses the diffracted sound more efficiently than on the edge on the source side. It is noticeable that the interval between secondary sources and error sensors has a significant influence on the magnitude of the quiet zone. There is a range of spacing for secondary sources and error sensors. When secondary sources are separated at intervals from

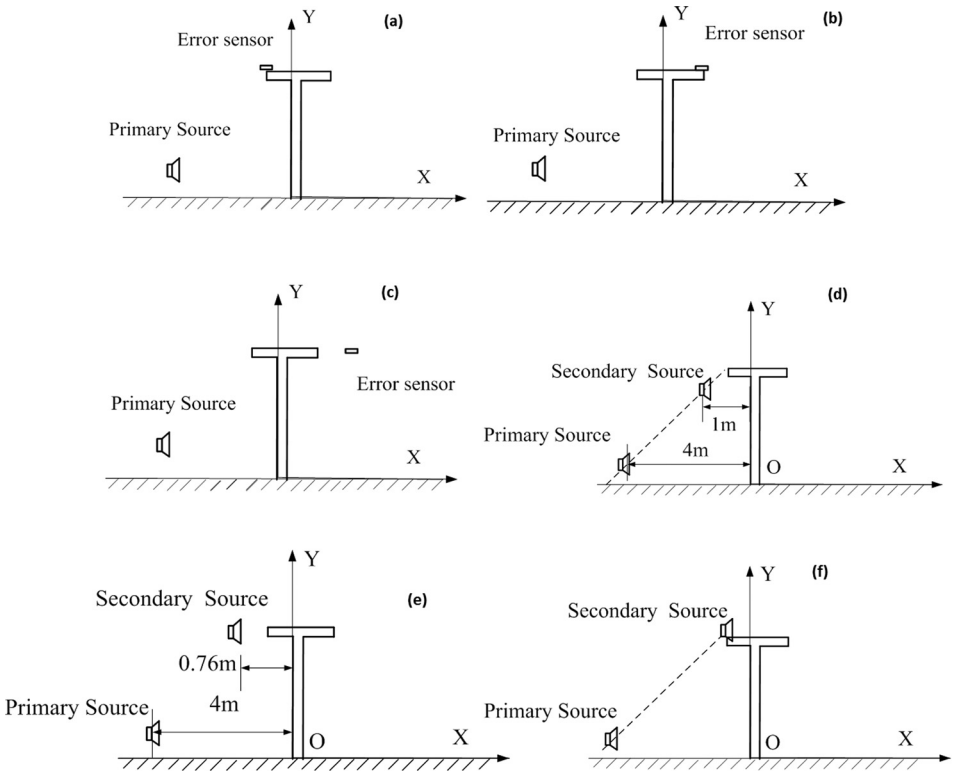

FIG. 9. Error sensors and secondary sources located at three positions: (a) Error sensors at location A on the edge on the receiving side, (b) error sensors at location B on the edge on the source side, (c) error sensors at location C behind T-shape noise barrier, (d) secondary sources at position SA at a distance of 1 m from the noise barrier, (e) secondary sources at position SB, and (f) secondary sources at position SC on the edge on the source side.

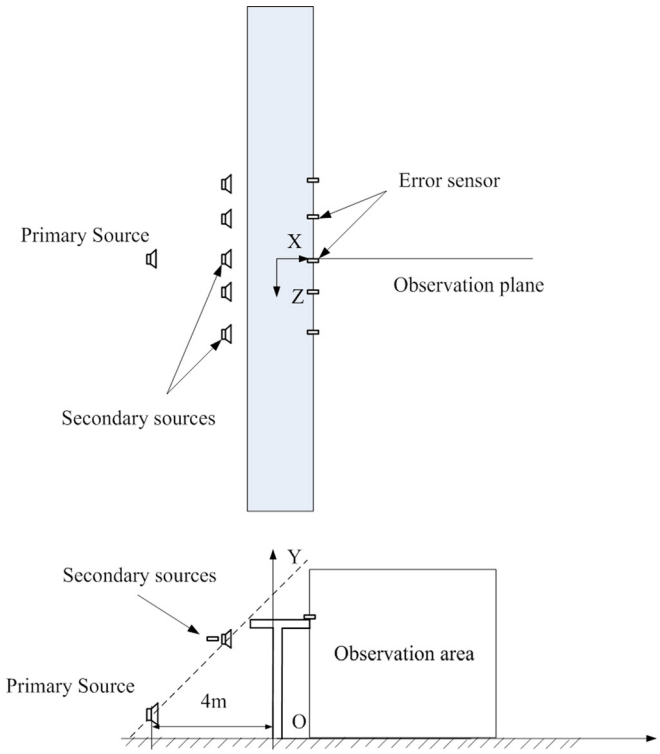

FIG. 10. (Color online) Active noise system configuration.

0.4 to 0.7 m, a larger quiet zone is created in the desired location behind the T-shaped barrier, as illustrated in Figs. 11(a)–11(d) and 12(b)–12(e). The largest quiet zone is obtained when error sensors are located at the edge on the receiving side at intervals of 0.6 m, as shown in Fig. 12(d).

C. Influence of location of secondary sources

For the different configurations with secondary sources at the three locations, the interval of 0.5 m between the error sensors is chosen and the error sensors are located at position B. Pure tones at the frequencies of 125 and 250 Hz are chosen as the input signals. In the case of the secondary sources at two positions SB and SC, Fig. 13 shows the numerical simulation results of the extra insertion loss at 125 and 250 Hz. For the configurations with the secondary sources at positions SB and SC, the attenuation and amplification of the diffracted sound field behind the T-shaped noise barrier at two frequencies are very similar. In the case of the interval of 0.5 m, the quiet zones behind the T-shaped noise barrier at the height from 1.6 to 2.0 m in Figs. 13(a) and 13(c) at 125 Hz are smaller than that in Fig. 12(c), showing that secondary sources at location SA are more effective in reducing the diffracted sound field than those at either of the locations SB or SC. At the two frequencies of 125 and 250 Hz, the quiet zones below the height of 2.0 m in Figs. 13(c) and 13(d) are larger than those in

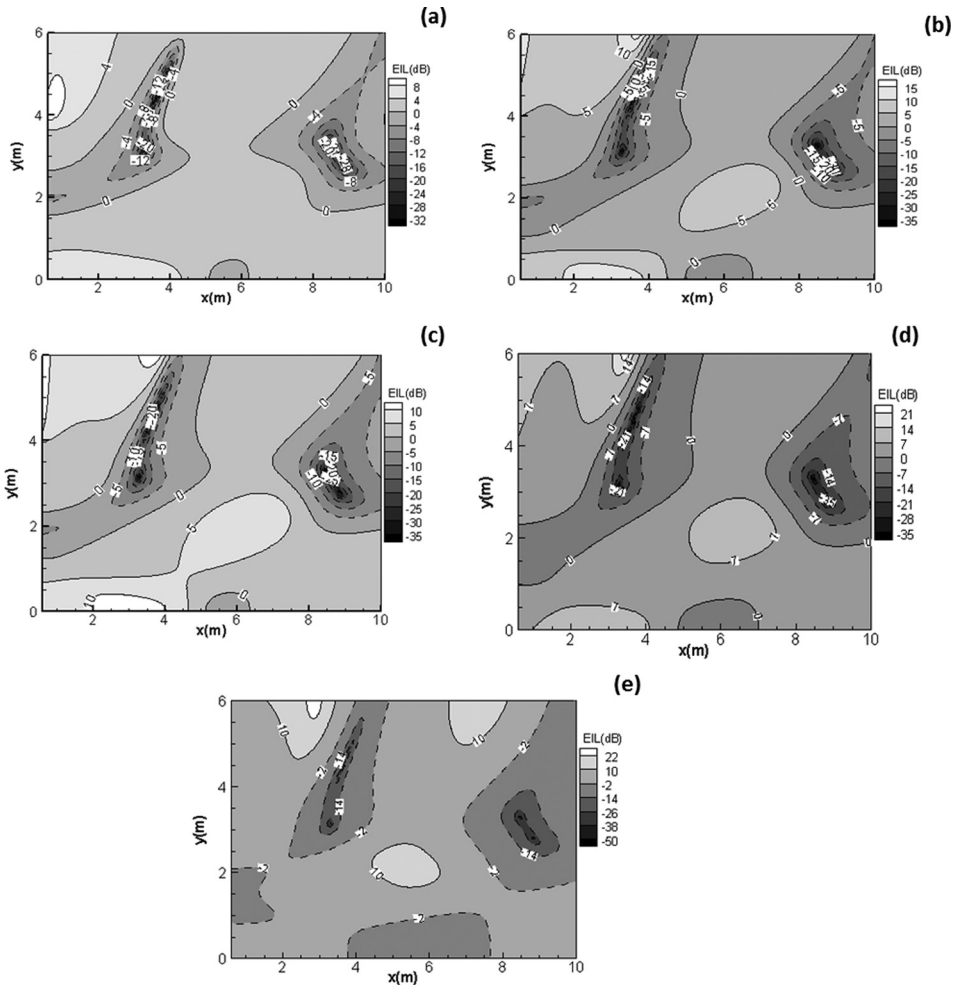

FIG. 11. Extra insertion loss of active noise control behind T-shape noise barrier for different spacings of error sensors with error sensors at location A: (a) 0.4 m, (b) 0.5 m, (c) 0.6 m, (d) 0.7 m, and (e) 1.4 m.

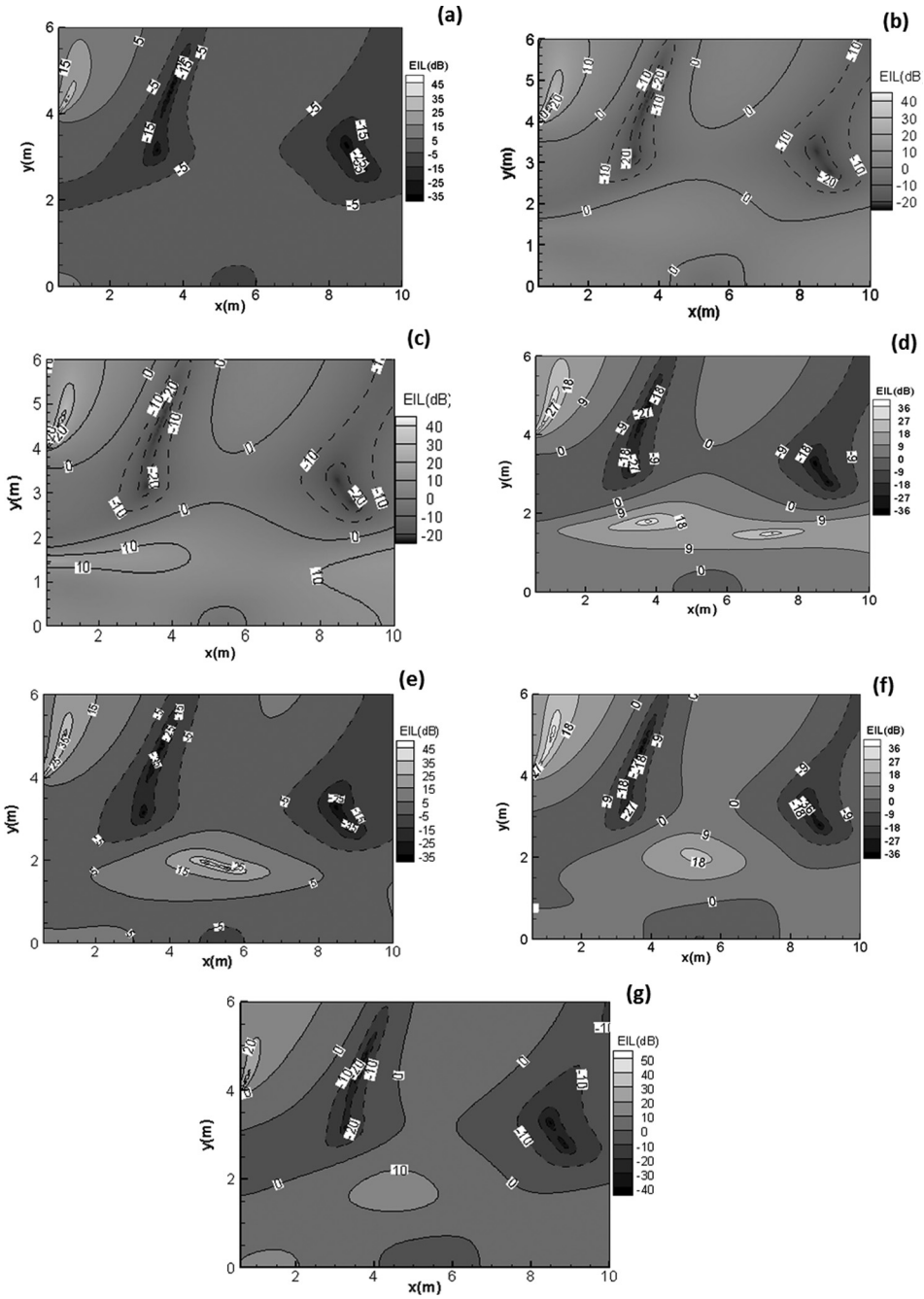

FIG. 12. Extra insertion loss of active noise control behind T-shape noise barrier for different spacing of error sensors with error sensors at location B: (a) 0.3 m, (b) 0.4 m, (c) 0.5 m, (d) 0.6 m, (e) 0.7 m, (f) 0.8 m, and (g) 1.4 m.

Figs. 13(a) and 13(b). It can be inferred that the location of the secondary sources at SC provides more effective control than at SB at these two frequencies.

IV. EXPERIMENTAL VALIDATION

Experiments are carried out in an anechoic chamber with dimensions 6 m × 6 m × 3 m. The metal-grid floor of the anechoic chamber is covered with wood plates to create the condition of rigid ground reflection. The performance of an active T-shaped noise barrier is investigated by 1:4 scale model experiments. The miniature T-shaped noise barrier is shown in Fig. 14. The barrier is made of plywood plates with a thickness of 0.05 m and a height of 1.0 m, and it is thick enough to prevent sound transmission in the investigated frequency range.

A simple minimax algorithm has faster convergence and better stability than FXLMS. The minimax algorithm can improve the uniformity in the residual acoustic field. With active noise control, the uniformity of the controlled acoustic field has an influence on the diffracted sound field. To obtain an even, uniform sound pressure field on the multiple error sensors, the minimax algorithm is used to minimize the sound pressure levels at the position of the error sensors.

A block diagram of the minimax active noise control is shown in Fig. 15. The electro-acoustic secondary path transfer function between the error microphone and the secondary source **S** was previously off-line identified by the system identification process of a conventional LMS algorithm. By unpacking the composite vector $\mathbf{w}(n)$ into the individual filters $\mathbf{w}_{ji}(n)$, $\mathbf{w}_{ji}(n)$ can be updated as

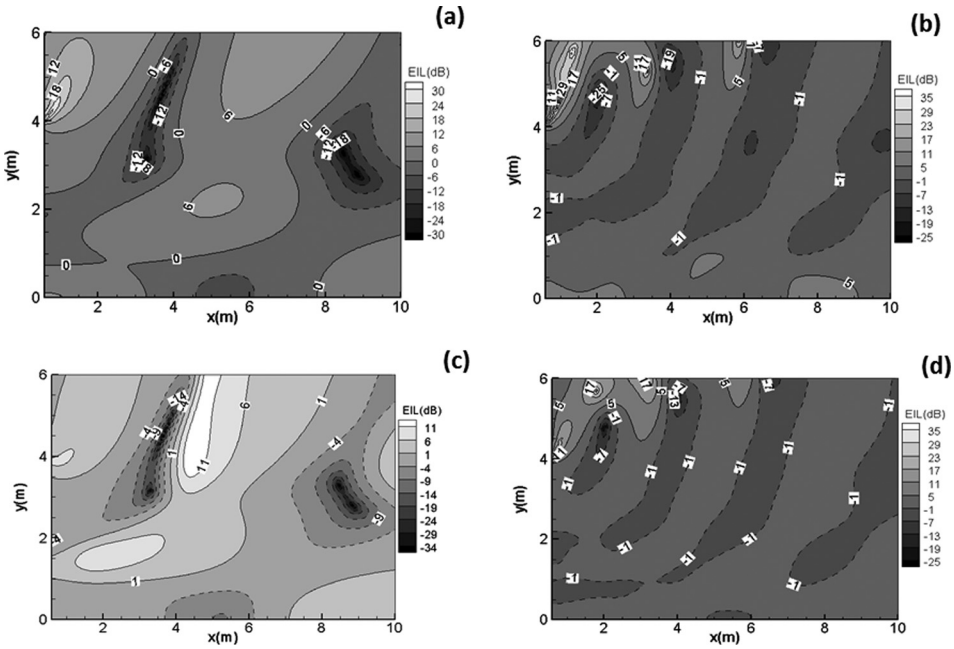

FIG. 13. Extra insertion loss of active noise control behind T-shape noise barrier with secondary sources at two locations SB and SC of: (a) at location SB, 125 Hz, (b) at location SB, 250 Hz, (c) at location SC, 125 Hz, and (d) at location SC, 250 Hz.

$$\mathbf{w}_{ji}(n+1) = \mathbf{w}_{ji}(n) + \mu \cdot e_b(n) \cdot \mathbf{r}_{bji}(n), \tag{18a}$$

where

$$\mathbf{r}_{bji}(n) = \hat{S}_{bj} * x_i. \tag{18b}$$

In the above, $\mathbf{w}_{ji}(n)$ stands for the ith filter coefficient for the jth secondary source, $e_b(n)$ is the error signal with the maximal magnitude in each interaction, and $\mathbf{r}_{bji}$ signifies the counterpart of the ith input signal (x_i) which is filtered by the measured electro-acoustic transfer function $\hat{S}_{bj}$ between the bth error sensor and the jth secondary source. μ is the step size parameter, and n is the sample number. The sampling frequency is 10 kHz. The number of taps used for the measured secondary path transfer function and adaptive filter $\mathbf{w}_j$ are 160 and 4, respectively. The identification and control procedure are implemented in the integrated environment of dSPACE and MATLAB's Real Time Toolbox.

The dSPACE system used for the adaptive control has a maximum of six output and ten input channels. The number of error sensors is limited by the capacity of the signal processing hardware. Therefore, the active control system consists of three loudspeakers used as secondary sources and three microphones used as error sensors. Pure tones at 500 Hz, 800 Hz, and 1000 kHz are used as the primary signals. The pure tone signal from the signal generator is sent directly to the primary source, and is also used as the reference signal of the control system. The sound pressure levels under the above conditions are measured with active noise control on and off. In the following part, the frequencies are converted from real values into quarter to facilitate the discussion.

For validating the influence of the different locations and intervals of the secondary sources and error sensors on control efficiency, the error sensors are located at three different positions: (a) Location A along the edge of the source side; (b) location B along the edge of the receiving side; (c) location C at a distance of 0.1 m from the edge, as shown in Figs. 9(a)–9(c). For comparison, the secondary sources at positions SA and SB, as shown in Figs. 14(a) and 14(b), are located along two lines ($x = -0.25$ m, $y = 0.8650$ m) and ($x = -0.125$ m, $y = 1.0$ m), respectively. The experimental setups are illustrated in Figs. 14(a) and 14(b). These configurations of the active control system have the following characteristics in common: Primary source at (−1, 0.125, 0 m).

For measuring the spatial contribution of extra insertion loss and comparison with the results of numerical simulation, three different sets of observation points behind the T-shape noise barrier are used for the configurations with

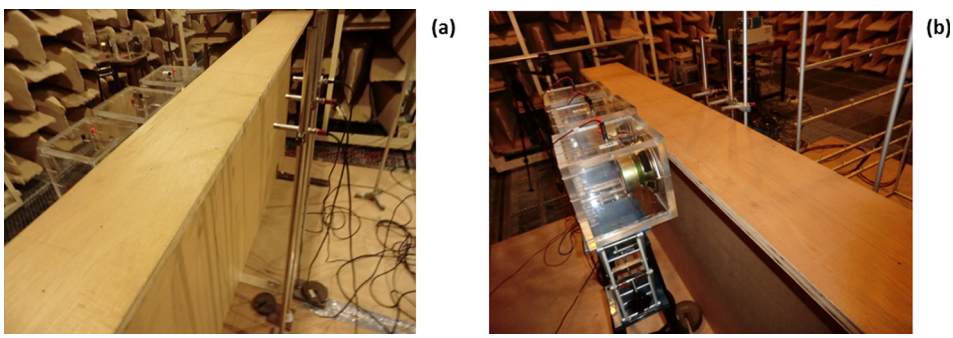

FIG. 14. (Color online) Photo of the active noise control system of T-shape noise barrier with different secondary sources: (a) Location SA and (b) location SB.

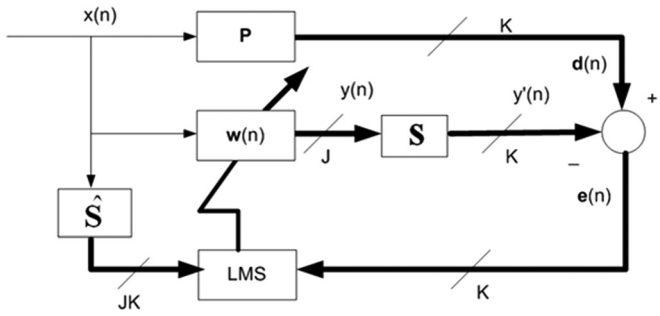

FIG. 15. Schematic representation of multiple-error feed-forward active noise control algorithm.

secondary sources at two different positions SA and SB, as shown in Figs. 16(a)–16(c). For the configuration with the secondary sources at location SA in Fig. 14(a), the extra insertion loss is measured for the two cases of the error sensors located at positions B and C. Measuring points are located at observation points $x = 1.0$, 1.5, 2.0, 2.5, 3.0 with $y = 0.5$ m and $z = 0$ m. The spacing of error sensors is 0.125 m.

For the secondary sources located at position SA with the error sensors located at positions B and C, the extra insertion loss at the observation points is demonstrated in Figs. 17(a) and 17(b). Positive values of the extra insertion loss indicate effective attenuation, and negative values indicate the increase in the sound pressure level by the active noise control. It can be seen that the location of the error sensors at position B on the edge of the receiving side is more efficient in reducing diffracted noise than the location of the error sensors away from the edge at position C.

Figure 17(a) shows that the active control works very effectively for 125, 200, and 250 Hz, with more than 3 dB attenuation at 250 Hz. As predicted by the numerical simulation in Fig. 12(c), attenuation in the sound pressure level in the area near 2.0 m is small at 125 Hz. At three frequencies, the experimental results of the extra insertion loss at five observation points with $y = 0.5$ m agree with the results of simulation. The noise attenuation at these observation points is greater at 250 Hz than at 125 Hz for the configuration with error sensors at position B, as shown in Fig. 17(a). These results clearly support the results of the numerical simulations.

For one configuration with secondary sources at location SB shown in Fig. 16(b), six observation points with coordinates P1 (0.5 m, 0.4 m), P2 (0.75 m, 0.4 m), P3 (0.5 m, 0.75 m), P4 (0.75 m, 0.75 m), P5 (0.5 m, 1.0 m), and P6 (0.75 m, 1.0 m) are used to measure the extra insertion loss in the near field when the error sensors are positioned at three locations A, B, and C. A pure tone at 250 Hz is used as the primary signal. Figure 17(c) shows the extra insertion loss in the near field for the 250 Hz tone for the configuration with the error sensors at three locations A, B, and C and the secondary sources at location SB. It is found experimentally

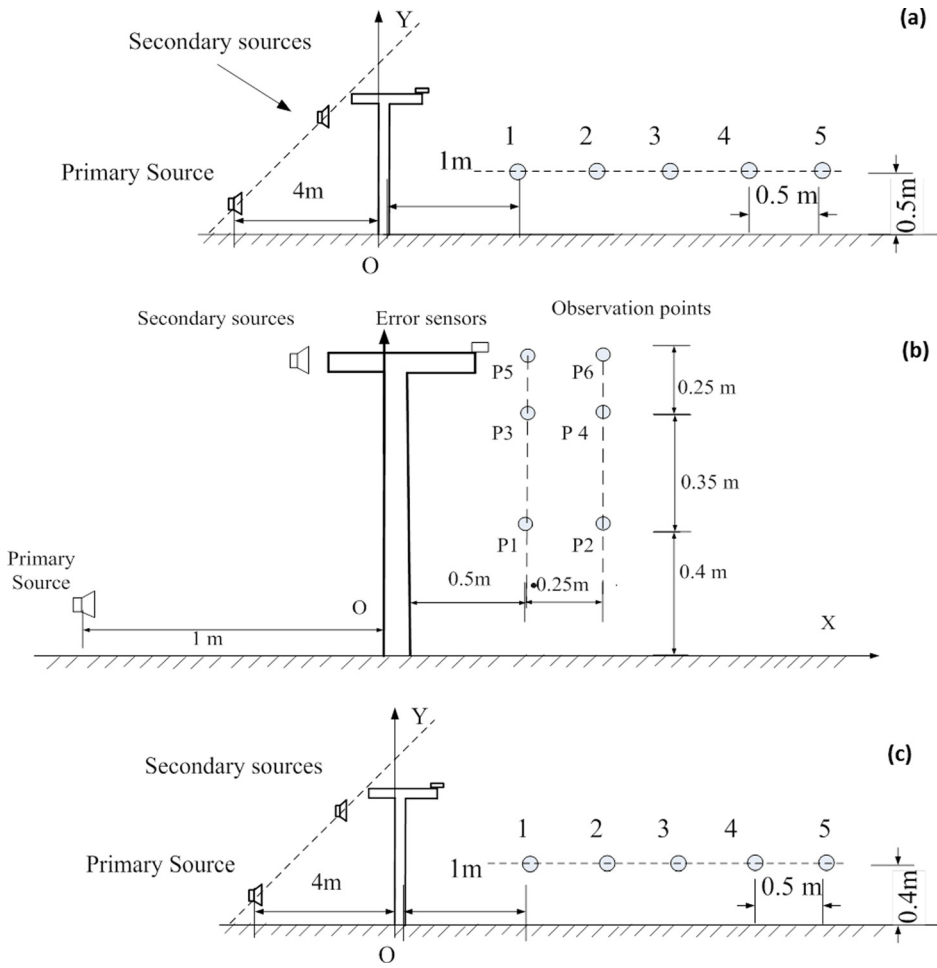

FIG. 16. (Color online) Schematic diagram of three sets of configurations in experiments: (a) Five observational points in the distance of 0.5 m from the ground, (b) six observational points, and (c) five observational points in the distance of 0.4 m from the ground.

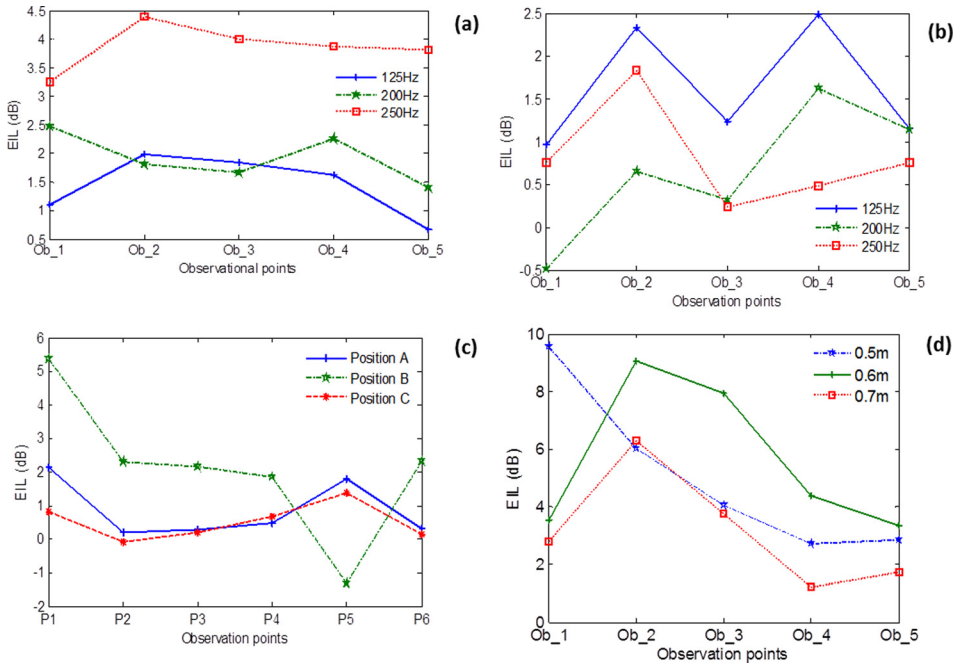

FIG. 17. (Color online) Experimental extra insertion losses in the observational points: (a) Error sensors on the edge of the receiving point, (b) error sensors in the distance of 0.1 m from the edge of observational points, (c) error sensors at three locations A, B, and C at 125 Hz, and (d) three separated distances of 0.5, 0.6, and 0.7 m in the observational points in the horizontal line $y = 0.4$ m.

that the error sensors at position B perform better in attenuation than those at positions A and C at a height of 2.0 m. These results also support the conclusions of the numerical simulation, namely that the reduction of sound pressure on the edge on the receiving side more effectively suppresses the diffracted sound field.

The separation distance between the error sensors is varied from 0.5 m to 0.7 m at intervals of 0.1 m to investigate the effect of the interval between the error sensors on the reduction efficiency. For the configuration with the error sensors on the receiving side of the T-shaped noise barrier and the secondary sources at position SA in Fig. 16(c), the distance between observation points and the ground was changed to 0.4 m. Figure 17(d) shows the sound attenuation measured in the horizontal line $y = 0.4$ m for the configuration with the error sensors on the edge of the receiving side as shown in Fig. 16(c). When the distance between error sensors is 0.5 m, the noise reduction at 125 Hz in the horizontal line $y = 0.4$ m is greater than that in Fig. 17(a). These results also support the results of the numerical simulation.

V. CONCLUSIONS

The insertion loss of a straight noise barrier and of T-shaped noise barriers with four surface conditions was investigated quantitatively. A T-shaped barrier with an acoustically soft surface was found to have the best capacity for reducing diffracted noise in the middle- or high-frequency range. The diffraction characteristics of acoustic fields of the T-shaped barrier were examined at three representative frequencies (125, 500, and 700 Hz). It could be observed from the sound pressure contours obtained and the equi-phase surfaces of the sound fields that each tip of the T-shaped barrier cap behaved as two imaginary edge sources to diffract sound wavefronts. It was also revealed that the mitigation of sound pressure around the right corner of the T-shaped barrier influenced the diffracted sound field in the observation area considerably. Using a minimax algorithm, different configurations of an active T-shape barrier with the secondary sources and the error sensors placed at various positions were interrogated. It was found that the spacing of the secondary sources and error sensors played a dominant role in creating quiet zones. Placement with the error sensor at the edge of the receiving side showed improved noise control efficiency compared with other configurations. Achieving an extra insertion loss of more than 3 dB, the minimax algorithm achieved a more even sound field distribution than obtained with the use of conventional FXLMS. The simulations were validated by experiments, both matching quantitatively. The actively controlled T-shaped noise barrier developed in this study presents advantages over traditional noise barriers, with great potential for use in urban areas to abate broadband noise in a cost-effective manner.

ACKNOWLEDGMENTS

Li Cheng is grateful to National Natural Science Foundation of China for a research grant (Grant No.: 11272272).

[1]T. Okubo and K. Fujiwara, "Efficiency of a noise barrier on the ground with an acoustically soft cylindrical edge," J. Sound Vib. **216**, 771–790 (1998).
[2]D. Greiner, J. J. Aznárez, O. Maeso, and G. Winter, "Single- and multi-objective shape design of Y-noise barriers using evolutionary computation and boundary elements," Adv. Eng. Software **41**, 368–378 (2010).
[3]T. Shizuka and K. Fujiwara, "Performance of noise barriers with various edge shapes and acoustical conditions," Appl. Acoust. **65**, 125–141 (2004).
[4]K. Fujiwara, D. C. Hothersall, and C.-H. Kim, "Noise barriers with reactive surfaces," Appl. Acoust. **53**, 255–272 (1998).
[5]M. R. Monazzam and Y. W. Lam, "Performance of profiled single noise barriers covered with quadratic residue diffusers," Appl. Acoust. **66**, 709–730 (2005).
[6]T. Okubo and K. Yamamoto, "Simple prediction method for sound propagation behind edge-modified barriers," Acoust. Sci. & Tech. **28**, 7–15 (2007).
[7]T. Okubo, T. Matsumoto, and K. Yamamoto, "Efficiency of edge-modified noise barriers: Intrinsic efficiency determination of practical

products and prediction of the diffracted sound field," Acoust. Sci. & Tech. **31**, 56–67 (2010).
[8]J. Defrance and P. Jean, "Integration of the efficiency of noise barrier caps in a 3D ray tracing method. Case of a T-shaped diffracting device," Appl. Acoust. **64**, 765–780 (2003).
[9]M. Baulac, J. Defrance, and P. Jean, "Optimization of multiple edge barriers with genetic algorithms coupled with a Nelder-Mead local search," J. Sound Vib. **300**, 71–87 (2007).
[10]S. Ise, H. Yano, and H. Tachibana, "Basic study on active noise barrier," J. Acoust. Soc. Jpn. (E) **12**, 299–306 (1991).
[11]N. Han and X. Qiu, "A study of sound intensity control for active noise barriers," Appl. Acoust. **68**, 1297–1306 (2007).
[12]A. Omoto, K. Takashima, and K. Fujiwara, "Active suppression of sound diffracted by a barrier: An outdoor experiment," J. Acoust. Soc. Am. **102**, 1671–1679 (1997).
[13]J. Shao, J. Z. Sha, and Z. L. Zhang, "The method of the minimum sum of squared acoustic pressures in an actively controlled noise barrier," J. Sound Vib. **204**, 381–385 (1997).
[14]D. Duhamel, "Improvement of noise barrier efficiency by active control," Acta Acust. **3**, 25–35 (1995).
[15]J. Tao, H. Zou, and X. Qiu, "Roof structure design in active noise barrier," *The 17th International Congress On Sound and Vibration*, Cairo (2010), pp. 18–22.
[16]J. Guo, J. Pan, and C. Bao, "Actively created quiet zones by multiple control sources in free space," J. Acoust. Soc. Am. **101**, 1492–1501 (1997).
[17]J. Guo and J. Pan, "Further investigation on actively created quiet zones by multiple control sources in free space," J. Acoust. Soc. Am. **102**, 3050–3053 (1997).
[18]J. Guo and J. Pan, "Increasing the insertion loss of noise barriers using an active-control system," J. Acoust. Soc. Am. **104**, 3408–3416 (1998).
[19]F. Niu, H. Zou, X. Qiu, and M. Wu, "Error sensor location optimization for active soft edge noise barrier," J. Sound Vib. **299**, 409–417 (2007).
[20]S. J. Elliott, I. M. Stothers, and P. A. Nelson, "A multiple error LMS algorithm and its application to the active control of sound and vibration," IEEE Trans. Acoust., Speech, Signal Process. **35**, 1423–1434 (1987).
[21]S. J. Elliott, C. Boucher, and P. A. Nelson, "Behavior of a multiple channel active control system," IEEE Trans. Acoust., Speech, Signal Process. **40**, 1041–1052 (1992).
[22]A. Gonzalez, A. Albiol, and S. J. Elliott, "Minimization of the maximum error signal in active control," IEEE Trans. Acoust., Speech, Signal Process. **1**, 387–390 (1997).
[23]A. Gonzalez, A. Albiol, and S. J. Elliot, "Minimization of the maximum error signal in active control," IEEE Trans. Acoust., Speech, Signal Process. **6**, 268–290 (1998).
[24]A. Gonzalez, A. Albiol, and S. J. Elliot, "Adaptive minimization of the maximum error signal in an active control system," IEEE ASSP Workshop on Applications of Signal Processing to Audio and Acoustics (1995), pp. 53–56.
[25]C. W. Lim, C. Cheong, S.-R. Shin, and S. Lee, "Time domain numerical computation of noise reduction by diffraction and finite impedance of barriers," J. Sound. Vib. **268**, 385–401 (2003).
[26]M. E. Delany and E. N. Bazley, "Acoustical properties of fibrous absorbent materials," Appl. Acoust. **3**, 105–116 (1976).
[27]D. Chu and T. K. Stanton, "Higher-order acoustic diffraction by edges of finite thickness," J. Acoust. Soc. Am. **122**, 3177–3194 (2007).